

The Structure of Inhomogeneous Turbulence in Variable Density Nonpremixed Flames¹

K.K. Nomura and S.E. Elghobashi

Mechanical and Aerospace Engineering Department, University of California,
Irvine, CA 92717, U.S.A.

Communicated by Mark N. Glauser, Jean-Paul Bonnet, and Thomas B. Gatski

Received 5 January 1993 and accepted 4 May 1993

Abstract. Some observations concerning the structure of turbulence associated with an exothermic nonpremixed reacting flow are presented. Direct numerical simulations (DNS) with a resolution of 128^3 grid points and an initial Reynolds number $R_\lambda = 33$ provide data for the analysis. In these simulations the density varies with temperature and the resulting flow field is inhomogeneous. Conditional probabilities of the vorticity and rate-of-strain, three-dimensional visualization, and topological characteristics are presented and compared with those of a constant density flow. Initially, thermal expansion causes significant changes in the small-scale statistics. As the development continues, the statistics reflect the competing mechanisms of vortex stretching, dilatation, and baroclinic torque. Preferential alignment of the vorticity with the eigenvector associated with either the intermediate or most extensional principal strain is observed depending on the value of the local mixture fraction. Intermittent vortex structures tend to exist as sheets or ribbons rather than tubes due to the diminishing levels of vorticity and a change in the distribution and preferential orientation of the principal strains. Topological characteristics not present in constant density flows are observed. However, as the flow develops and the divergence decreases, the topology becomes similar to those of incompressible turbulence.

1. Introduction

Descriptions of the small-scale structure of homogeneous turbulence have recently been provided by examining correlations of vorticity and strain-rate from direct numerical simulation (DNS) results (Ashurst *et al.*, 1987; She *et al.*, 1991; Ruetsch and Maxey, 1991; Vincent and Meneguzzi, 1991). Structural characteristics are deduced from conditional probabilities and direct three-dimensional visualization. As reported in these studies, incompressible homogeneous turbulence appears to consist of intermittent coherent structures embedded in a random background field. The vortex structures are tube-like at high-vorticity regions and sheet-like at moderate-vorticity regions. There is preferential alignment of vorticity with the eigenvector corresponding to the intermediate principal rate-of-strain which is found to be predominantly positive. Amplification of vorticity thus takes place by stretching along the direction of the intermediate eigenvector with the two larger strains residing in

¹ This research was supported in part by an award from the Universitywide Energy Research Group (UERG). A portion of the allocation at SDSC was provided by the University of California, Irvine. The first author also received support through a President's Dissertation Year Fellowship from the University of California.

the perpendicular plane. The preferred alignment and positivity of the intermediate eigenvector and associated eigenvalue are exhibited by both unsheared and sheared flows, and have also been found experimentally, at least for moderate Reynolds numbers (Tsinober *et al.*, 1992). These observations describe characteristics associated with intermittency in turbulent flows and may suggest a universal structure of the small scales.

In a chemically reacting flow, knowledge of small-scale structure is essential in understanding the turbulent mixing and reaction processes. In a previous investigation (Nomura and Elghobashi, 1992), the small-scale structure of turbulence in a nonpremixed reacting flow with negligible chemical energy release (constant density) was investigated. Both homogeneous isotropic (grid) and sheared turbulence were considered. The reactant field is passive and decoupled from the flow field which therefore remains homogeneous. The observed small-scale features of the flow field are in agreement with results of previous studies. Analysis of the passive scalar field showed that the gradient of the conserved scalar tends to align with the most compressive strain direction and orthogonal to the local vorticity. Regions of high scalar gradient magnitude and scalar dissipation tend to exist as sheets in the vicinity of the sheet-like vortex structures. It is at these regions where reaction rates will likely be highest.

In a nonpremixed reaction with *exothermic energy release*, the reacting scalar is no longer passive and the velocity and scalar fields are coupled through the varying density field. In this case the flow field is no longer homogeneous or strictly incompressible. The additional mechanisms present in this flow are indicated by the vorticity transport equation:

$$\frac{D\omega}{Dt} = (\omega \cdot \nabla)u - \omega(\nabla \cdot u) + \frac{(\nabla\rho \times \nabla p)}{\rho^2} + \nu \nabla^2 \omega. \quad (1)$$

The four terms on the right-hand side of (1) describe, respectively, vortex stretching, volumetric expansion (or compression), baroclinic torque, and viscous diffusion. In terms of enstrophy, ω^2 :

$$\frac{D}{Dt}(\frac{1}{2}\omega^2) = \omega \cdot S \cdot \omega - \omega^2(\nabla \cdot u) + \omega \cdot \frac{(\nabla\rho \times \nabla p)}{\rho^2} + \nu \nabla^2(\frac{1}{2}\omega^2) - \nu \nabla\omega : (\nabla\omega)^T, \quad (2)$$

where there is the additional mechanism of viscous dissipation (the last term). In a constant-density flow, the dilatation and baroclinic terms are zero. It is therefore these two mechanisms that distinguish the variable-density flow from the constant-density flow. Volumetric expansion or dilatation occurs when the density decreases due to heating by the exothermic energy. Since the velocity divergence ($\nabla \cdot u$) is positive for an expanding flow, the term $-\omega^2(\nabla \cdot u)$ represents a decrease in enstrophy. The baroclinic torque represents the generation (or destruction) of vorticity due to the interaction of density gradients with the local pressure gradient or fluctuations in the pressure field. Since the term is defined by the vector cross product of the density and pressure gradients ($\nabla\rho \times \nabla p$), it is nonzero when the two vectors are misaligned. Although phenomena such as "flame-generated" turbulence has been reported for reacting flows, it is generally known that, for nonpremixed reactions, the overall effect of chemical energy release is to reduce the intensity of turbulent fluctuations (Bilger, 1989; McMurtry *et al.*, 1989).

With these additional processes acting on the vorticity field, it is of interest to determine to what extent the reported small-scale properties are modified. The main objective of this study is to examine the structural characteristics of the vorticity and strain-rate fields under variable-density conditions which, in this case, are produced by exothermic energy release. Details of the active scalar mixing field will be described in a separate article (Nomura and Elghobashi, 1993).

2. Direct Numerical Simulations

Direct numerical simulations of a turbulent nonpremixed reacting flow with exothermic energy release was used to generate the data for the present analysis. The computational domain and initial conditions are depicted in Figure 1. The flow field is initially homogeneous isotropic turbulence which subsequently develops due to the density variation in the reaction zone. The limiting case of zero

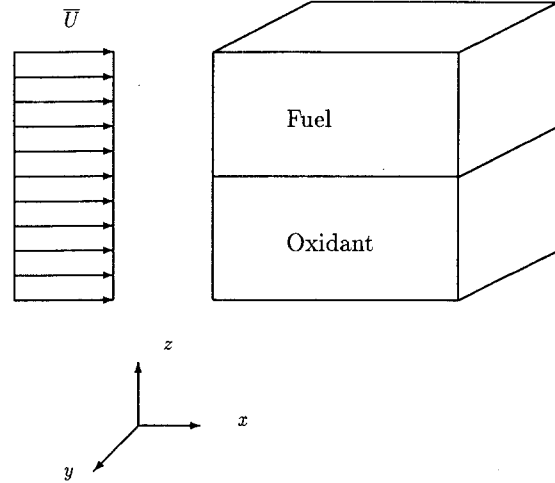


Figure 1. Computational domain and initial scalar distribution.

Mach number compressible flow is considered, in which the density varies only with temperature and not pressure.

We consider a simple one-step irreversible chemical reaction: $A + B \rightarrow C + \text{energy}$, where A and B denote nonpremixed fuel and oxidant, respectively, and C denote products. An infinite reaction rate is assumed so that the reaction is mixing rate limited. Both fuel and oxidant are assumed to have equal diffusivities (equal Schmidt number Sc). These assumptions allow a linear combination of the equations describing the conservation of the mass fractions of the two reactants to yield an equation for a conserved scalar (Burke and Schumann, 1928; Zeldovich, 1949). The conserved scalar in this case is the mixture fraction, F , and is defined by

$$F \equiv \frac{\varphi - \varphi_2}{\varphi_1 - \varphi_2}, \quad (3)$$

where φ is a Shvab–Zeldovich variable and $\varphi \equiv m_A - m_B/r$, where m_A and m_B are the mass fractions of fuel and oxidant, respectively. The quantity r is the mass of oxidant per unit mass of fuel required for complete reaction. The subscripts 1 and 2 denote the two initial homogeneous reactant streams. With the additional assumptions of unity Lewis number ($Le = Sc/Pr = 1$) and negligible $\partial p/\partial t$ in the energy equation, the form of the enthalpy and mixture fraction transport equations will be the same. The solutions are therefore similar and the enthalpy can be directly related to the mixture fraction:

$$F = \frac{h - h_2}{h_1 - h_2}. \quad (4)$$

By applying (4), the instantaneous temperature can be linearly related to the instantaneous mixture fraction. At the stoichiometric mixture fraction, F_{st} , the flame sheet exists and the temperature is the adiabatic flame temperature, T_{ad} . For $F < F_{st}$, no fuel is present and the following relationship holds:

$$\frac{T}{T_0} = (\tau - 1) \frac{F}{F_{st}} + 1. \quad (5)$$

For $F > F_{st}$, no oxidant is present and

$$\frac{T}{T_0} = (\tau - 1) \frac{1 - F}{1 - F_{st}} + 1, \quad (6)$$

where T_0 is the reference (ambient) temperature and $\tau = T_{ad}/T_0$ is a dimensionless heat-release parameter. Equations (5) and (6) provide explicit evaluation of temperature based on the computed mixture fraction and therefore eliminates the need to solve the energy equation directly.

The governing equations are the three-dimensional, time-dependent Navier–Stokes, continuity, and mixture fraction equations describing a variable-density flow in the limit of zero Mach number. In

nondimensional form they are:

$$\frac{\partial \rho}{\partial t} + \frac{\partial \rho u_j}{\partial x_j} = 0, \quad (7)$$

$$\frac{\partial \rho u_i}{\partial t} + \frac{\partial \rho u_i u_j}{\partial x_j} = -\frac{\partial p}{\partial x_i} + \frac{1}{Re} \frac{\partial}{\partial x_j} \left\{ \frac{\partial u_i}{\partial x_j} + \frac{\partial u_j}{\partial x_i} - \frac{2}{3} \delta_{ij} \frac{\partial u_k}{\partial x_k} \right\}, \quad (8)$$

$$\frac{\partial \rho F}{\partial t} + \frac{\partial \rho u_j F}{\partial x_j} = \frac{1}{Sc} \frac{\partial^2 F}{\partial x_j^2}, \quad (9)$$

where standard nomenclature is used. Note that the time t is nondimensionized by L/U , where L is the length of the computational box and U is a characteristic velocity. The equations are coupled through the density ρ which is determined by the equation of state using the evaluated temperature (5)–(6) and an assumed constant thermodynamic pressure, P_0 . It is important to realize that while the thermodynamic pressure P_0 , which is a zero-order quantity in a small Mach number expansion, is assumed constant, the *dynamic* pressure p is a first-order quantity which varies and is thus retained in the equations (see, for example, Paolucci, 1982).

The computational domain is a cube with 128^3 grid points. Periodic boundary conditions are used in the horizontal (x, y) directions due to spatial homogeneity in these directions. The resulting thermal expansion from energy release require outflow boundary conditions in the vertical (z) direction. The following advective boundary condition was developed for this purpose:

$$\frac{\partial(\rho u_i)}{\partial t} + \bar{W} \frac{\partial(\rho u_i)}{\partial z} = 0, \quad (10)$$

where \bar{W} is the mean z -component velocity at the outflow plane. The effectiveness of this boundary condition was tested by performing simulations in which the computational domain was extended by one full box length in both z -directions. The results showed no significant differences in statistical quantities describing the interior (heated) region of the flow field for the extent of the simulations.

The simulations are initialized with a fully developed isotropic turbulent velocity field ($R_\lambda = 33$) obtained from simulations using periodic boundary conditions in all three directions (Nomura and Elghobashi, 1992). As shown in Figure 1, the initial conditions for the conserved scalar (F) field is a step profile in the z -direction which represents two separate streams of (nonpremixed) reactants. The initial temperature and density are uniform at the reference values, T_0 and ρ_0 , respectively.

The overall numerical solution scheme is based on a second-order finite-difference method originally developed for constant-density flow (Gerz *et al.*, 1989) and later modified to allow variable density (Momtaz, 1990). Other details of the general method are provided in Nomura and Elghobashi (1992). The accuracy of the numerical scheme has previously been tested for homogeneous flows. In terms of resolving the small scales, since the Kolmogorov scale continually increases in the flows considered, resolution improves with time and thus it is sufficient that the resolution requirement be checked only initially (Nomura and Elghobashi, 1992). Eventually, the growth of scales reaches a point in which the boundary conditions are no longer valid. The duration of the simulations is therefore limited to a relatively early period of development.

3. Analysis and Results

Results of two simulations are presented, both with identical initial conditions. The first is a constant-density (no energy release) case provided for comparison; the second is the variable-density case with a value of the heat-release parameter, $\tau \equiv T_{ad}/T_0 = 1/\rho_{min} = 6$. It should be noted that the constant-density case corresponds to unforced grid turbulence and thus in both simulations, the turbulence decays in time.

General Turbulence Characteristics

We first present some general characteristics of the turbulent flow field. Statistical averages are computed over the volume of *active* fluid points defined as locations where the local scalar value indicates *mixed* fluid ($0.1 \leq F \leq 0.9$). Figure 2 shows instantaneous contours of the mixture fraction in

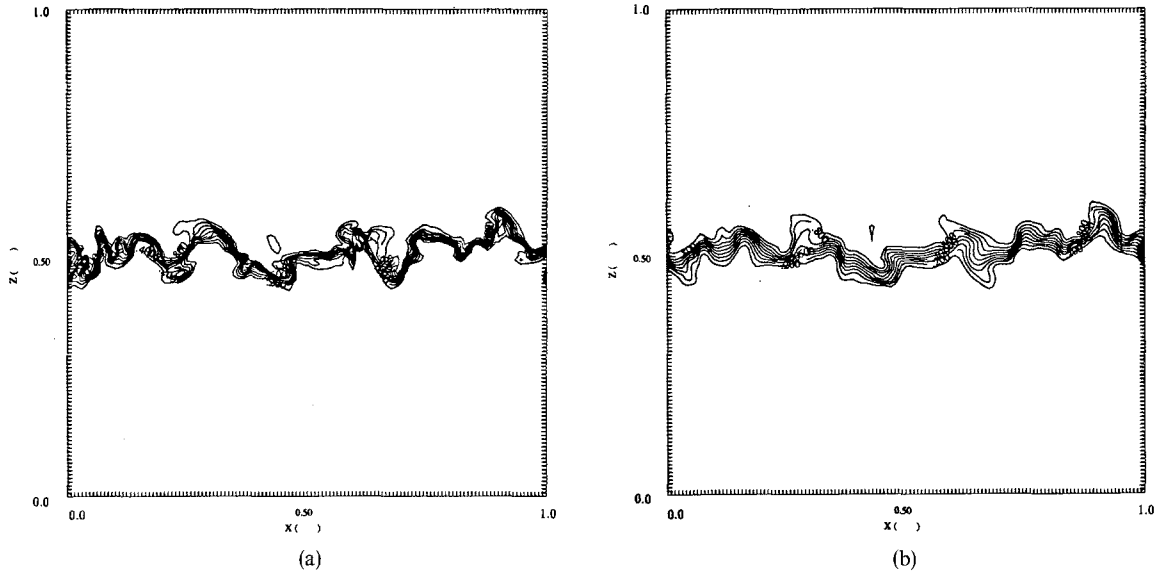


Figure 2. Instantaneous isoscalar contours ($0.1 \leq F \leq 0.9$) in a vertical $x-z$ plane ($y = L/2$) at $t = 3$: (a) no energy release, (b) with energy release.

a vertical ($x-z$) plane for the range $0.1 \leq F \leq 0.9$ indicating the relative extent of this zone. As expected, the presence of energy release causes a greater decrease in turbulent fluctuations than constant-density decay turbulence. The most rapid decrease occurs in the z -component of velocity where energy is transferred to the mean flow in this direction. The effect of the reduction in turbulence intensity can be seen in the scalar field (Figure 2(b)) which appears less convoluted than that of the constant-density case (Figure 2(a)).

Since the flow is inhomogeneous, length scales exhibit a spatial dependence. A length scale reflecting directionality is the Taylor microscale, λ_i , defined by

$$\lambda_i = \left(\frac{\langle u_i^2 \rangle}{\langle (\partial u_i / \partial x_i)^2 \rangle} \right)^{1/2}, \quad i = 1, 2, 3. \quad (11)$$

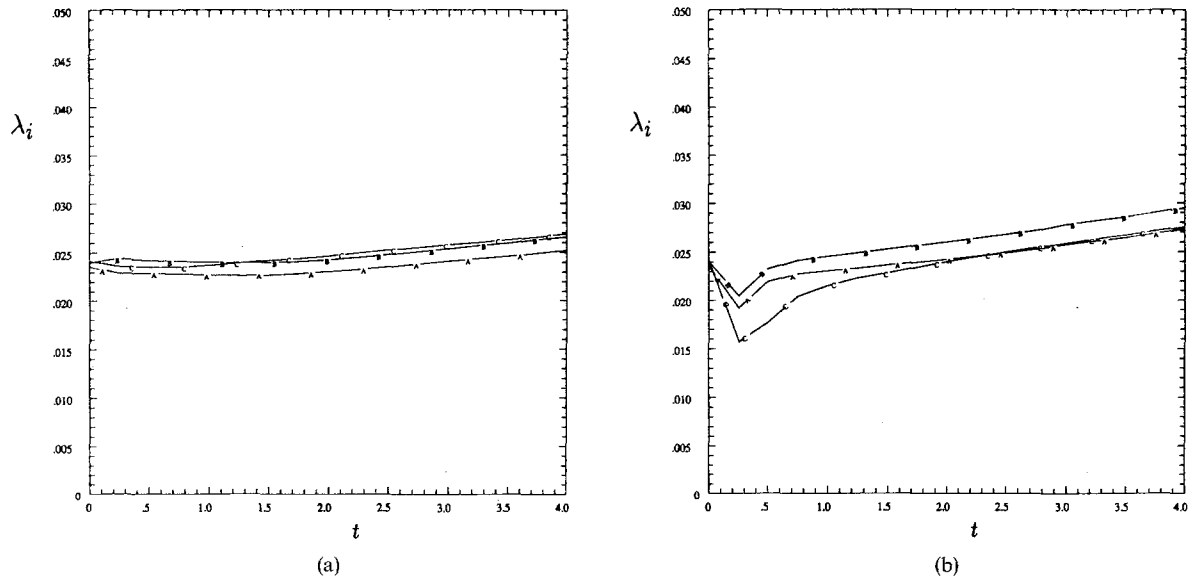


Figure 3. Time development of the Taylor microscale components λ_i (A: λ_1 , B: λ_2 , C: λ_3): (a) no energy release, (b) with energy release.

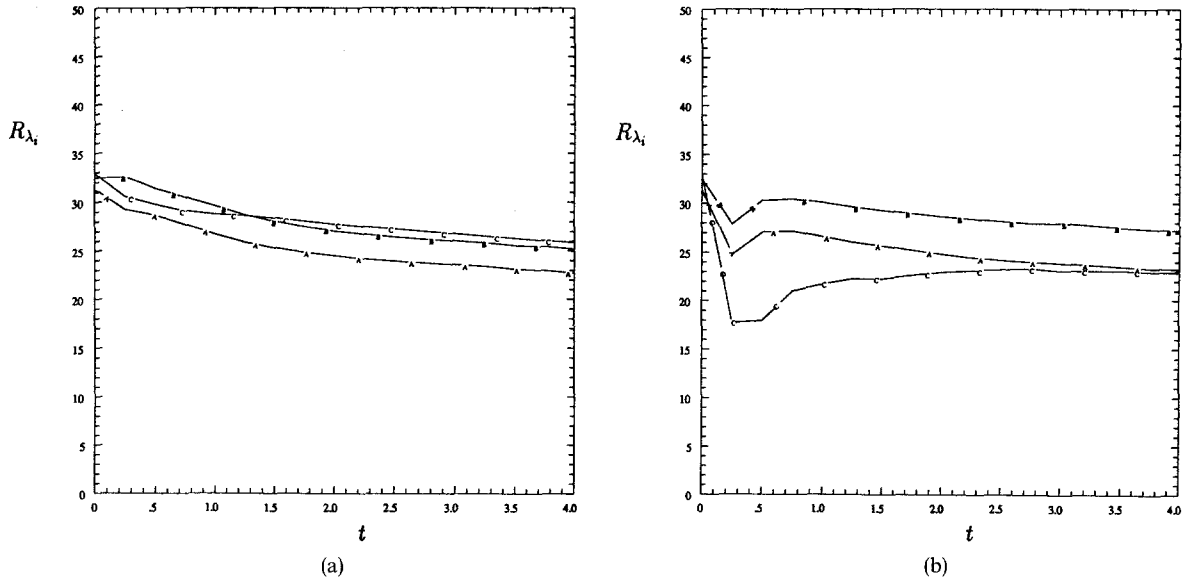


Figure 4. Time development of Reynolds number R_{λ_i} (A: R_{λ_1} , B: R_{λ_2} , C: R_{λ_3}): (a) no energy release (three-dimensional spectra), (b) with energy release (two-dimensional spectra at $z = L/2$).

The time development of λ_i (Figure 3) shows a greater rate of increase in the dissipation scales in the case of energy release due to the reduced strain magnitudes. This also indicates that dissipation is decreasing at a faster rate than the kinetic energy. The initial decrease (Figure 3(b)) is due to the dominating effect of expansion. A Reynolds number in terms of the Taylor microscale components ($R_{\lambda_i} = u_i \lambda_i / \nu$) is presented in Figure 4. We see that the values remain above 22 for time $t > 1$ and thus even in the case of energy release, the flow is still turbulent in the reaction zone.

Spectra of the energy and energy dissipation rate at a time $t = 3$ are shown in Figure 5. In the variable-density case (Figure 5(b)), since the flow is inhomogeneous, the spectra are two-dimensional and evaluated at the center horizontal plane ($z = L/2$). The profiles show the shift to lower wave

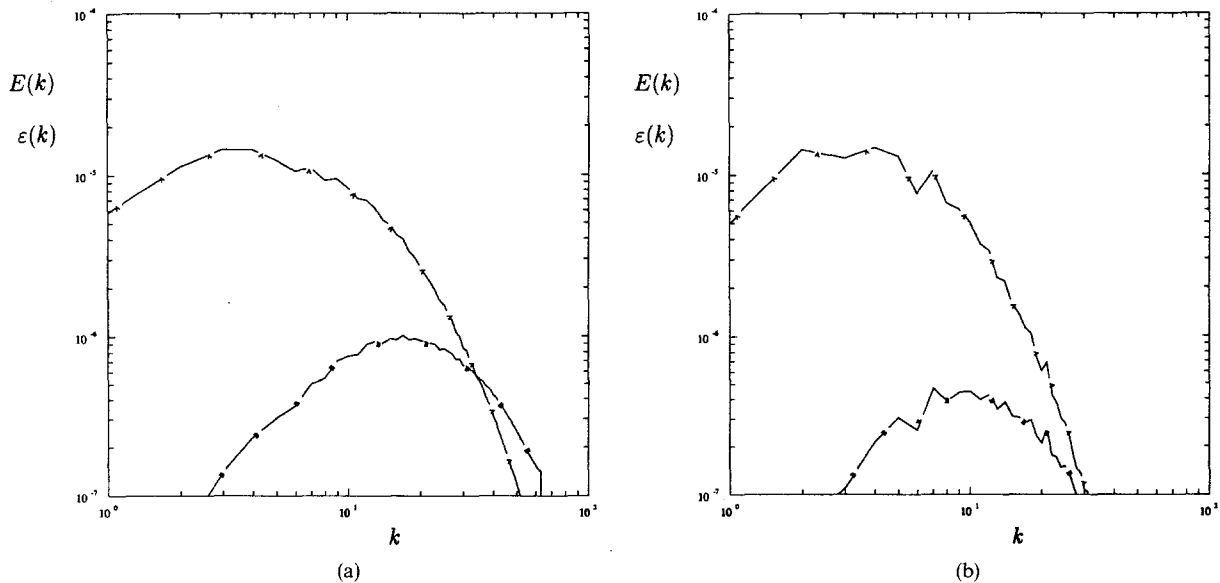


Figure 5. Spectra of the energy $E(k)$ (A) and energy dissipation rate $\epsilon(k)$ (B) at time $t = 3$ for (a) no energy release and (b) with energy release.

numbers (larger scales) in the heated flow. This is due to the growth of the Kolmogorov scales associated with the reduced dissipation rate indicating a decrease of enstrophy in the flow.

Vorticity and Strain Statistics

Since we are interested in small-scale features of the flow, we consider those quantities relating to the gradient of the velocity and not the velocity itself. As discussed in Batchelor (1967), the velocity-gradient tensor A_{ij} can be decomposed into a symmetric and antisymmetric part:

$$A_{ij} = \frac{\partial u_i}{\partial x_j} = S_{ij} + R_{ij}, \quad (12)$$

where $S_{ij} = \frac{1}{2}(\partial u_i/\partial x_j + \partial u_j/\partial x_i)$ is the rate-of-strain tensor (symmetric) and $R_{ij} = \frac{1}{2}(\partial u_i/\partial x_j - \partial u_j/\partial x_i)$ is the rate-of-rotation tensor (antisymmetric) and equal to one-half the vorticity ω_k . The vorticity vector ω and rate-of-strain tensor S are evaluated from the spatial derivatives of the DNS velocity fields at each grid point.

The rate-of-strain can be characterized by the principal eigenvalues and associated eigenvectors. The eigenvalues are determined from the characteristic equation

$$\lambda^3 + I_s \lambda^2 + II_s \lambda + III_s = 0, \quad (13)$$

where the coefficients I_s , II_s , and III_s are the principal invariants which may be written as (Aris, 1989; Lumley, 1970)

$$I_s = -S_{ii}, \quad (14)$$

$$II_s = \frac{1}{2}(S_{ii}^2 - S_{ij}S_{ji}), \quad (15)$$

$$III_s = -\frac{1}{3!}(S_{ii}^3 - 3S_{ii}S_{jk}S_{kj} + 2S_{ij}S_{jk}S_{ki}). \quad (16)$$

The λ 's are computed from (13) and designated by the convention $\alpha \geq \beta \geq \gamma$. The eigenvectors corresponding to α , β , γ are referred to as e_α , e_β , and e_γ , respectively. The invariants may also be expressed in terms of the eigenvalues:

$$I_s = -(\alpha + \beta + \gamma), \quad (17)$$

$$II_s = \alpha\beta + \alpha\gamma + \beta\gamma, \quad (18)$$

$$III_s = -\alpha\beta\gamma. \quad (19)$$

Various conditional probabilities involving vorticity and the principal rates of strain are evaluated in order to characterize the flow structure. As previously mentioned, a base sample volume consisting only of active fluid points is defined. From this base sample, further conditioning is imposed where stated. However, because of the inhomogeneity of the flow field, the dependency on the value of F is also considered.

For constant-density (no energy release) flows, the incompressibility condition ($\nabla \cdot u = 0$) requires that $\alpha + \beta + \gamma = 0$, or $I_s = 0$. In this case, α is always positive (most extensional strain), γ is always negative (most compressive strain), and β is either positive or negative (intermediate) depending on the magnitudes of α and γ . Furthermore, if a scatter plot of normalized α versus β (normalized by $|e| = \sqrt{\alpha^2 + \beta^2 + \gamma^2}$) was made, all points would fall on a curve given by

$$\alpha = \frac{-\beta + \sqrt{2 - 3\beta^2}}{2}, \quad (20)$$

where the limits of β are $-1/\sqrt{6} \leq \beta \leq 1/\sqrt{6}$. A similar relationship can also be derived for γ versus β . These relationships arise due to the incompressibility constraint and the chosen normalization factor $|e|$ and indicate that, for a given value of normalized β , a unique value of α and γ exists. Figure 6(a) shows the probability distribution of the normalized principal strain-rates which exhibits the most probable ratio of $\alpha:\beta:\gamma$ as approximately 3:1:-4, in agreement with Ashurst *et al.* (1987) and Kerr (1987). As explained above, this is equivalent to a probable value of $\beta = 0.2$ (Kerr, 1987). Regions of points with $\beta > 0$ comprise 75% of the total volume and give an average value of $\bar{\beta} = 0.1$.

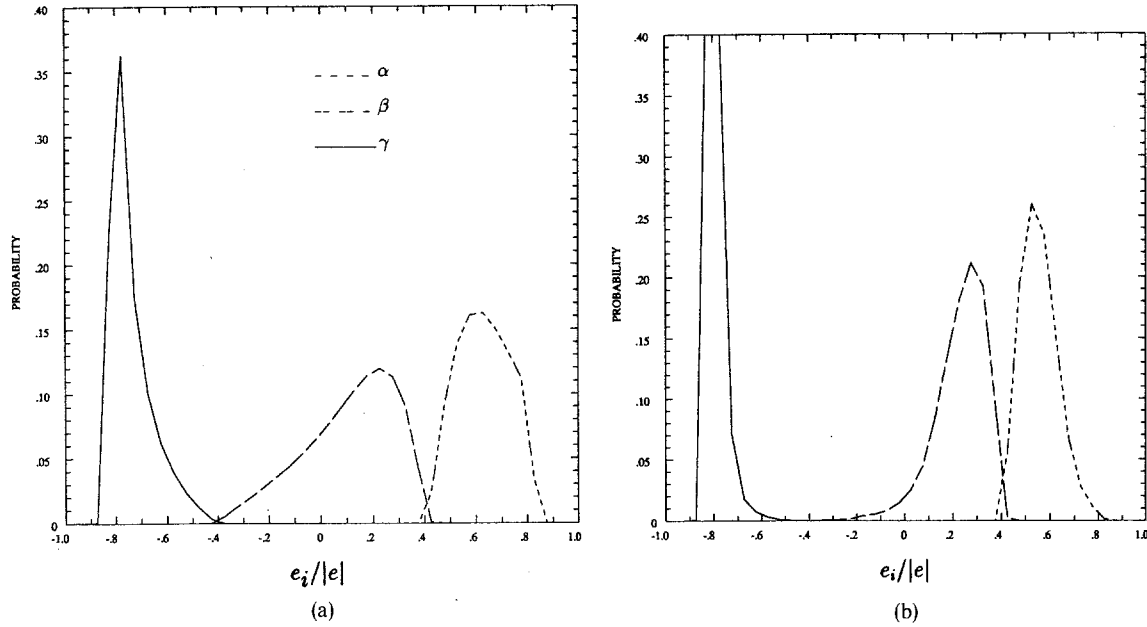


Figure 6. Probability distributions of the principal strain rates (normalized by total strain magnitude, $|e| = (\alpha^2 + \beta^2 + \gamma^2)^{1/2}$) for a flow with no energy release (constant density): (a) base sample ($0.1 \leq F \leq 0.9$), (b) high strain magnitude regions ($e^2 > 4\bar{e}^2$); —, γ ; ---, β ; ·····, α .

The distribution is somewhat sensitive to the magnitude of enstrophy of the sample. If the sample is limited to only those locations of relatively high enstrophy ($\omega^2 > 8\bar{\omega}^2$), the percentage of points with $\beta > 0$ increases to 80–85%. If the sample includes only high strain points ($e^2 > 4\bar{e}^2$) however, a more significant increase in positive β values (95–99%) is observed (Figure 6(b)). The average values of the eigenvalues give a ratio close to 3:1:–4. This result is also obtained when the sample is limited to locations where $\beta > 0$.

In the case of a variable density flow (with energy release), the presence of a nonzero velocity divergence ($\nabla \cdot v \neq 0$) causes the sum of the principal eigenvalues to be finite ($I_s \neq 0$). Early in the development of the nonpremixed reaction with energy release, significant positive divergence exists due to thermal expansion. This causes a corresponding shift in the distribution of eigenvalues toward positive values (Figure 7(a)). Note the overlap of the three curves and the possibility of $\gamma > 0$ which are not present in the constant-density case (the slight overlap in Figure 6 is due to finite bin width in calculating the statistics). The most probable ratio at this time ($t = 0.5$) is approximately 3:1:–2. This indicates that the largest strain magnitude tends to be extensional rather than compressive as in the constant-density case. As the development continues (Figure 7(b)), the level of divergence diminishes and the distribution appears to shift toward that of constant-density flow. A positive shifted distribution like that of Figure 7(a), however, remains at those locations with significant velocity divergence. If we again limit the sample to high strain magnitude ($e^2 > 4\bar{e}^2$) locations, the percentage of points with positive β is reduced to about 72–78% (Figure 7(c)). We see that positive divergence is not associated with the highest strain regions of the flow. The eigenvalue distribution shown more closely resembles that of the constant-density case and the average values give a ratio close to 3:1:–4. This preferred distribution seems to be associated with the activity of enstrophy production (vortex stretching) which, in a reacting flow with energy release, tends to dominate over the thermal expansion process at high strain regions and at later times.

The eigenvalue distribution can also be examined in terms of the invariants of S_{ij} (17)–(19). Figure 8 shows scatter plots of the invariant plane II_s – III_s and consists of data from six (x – z) planes. In the space of the invariants, the complex and real solutions are separated by a surface which can be written in the form given by Chong *et al.* (1990):

$$27III_s^2 + (4I_s^3 - 18I_sII_s)III_s + (4II_s^3 - I_s^2II_s^2) = 0. \quad (21)$$

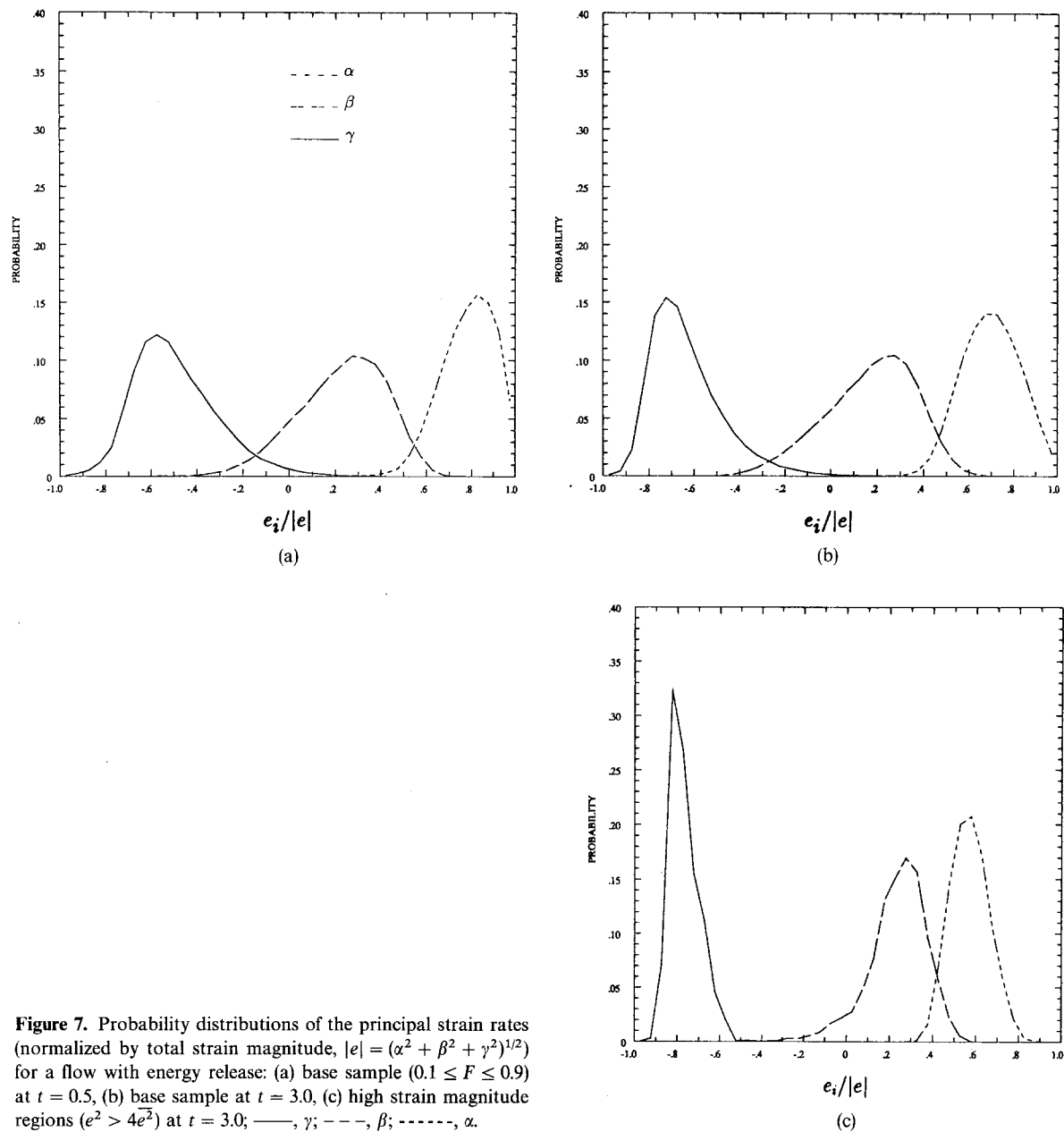


Figure 7. Probability distributions of the principal strain rates (normalized by total strain magnitude, $|e| = (\alpha^2 + \beta^2 + \gamma^2)^{1/2}$) for a flow with energy release: (a) base sample ($0.1 \leq F \leq 0.9$) at $t = 0.5$, (b) base sample at $t = 3.0$, (c) high strain magnitude regions ($e^2 > 4e^2$) at $t = 3.0$; —, γ ; ---, β ; - · - · -, α .

Since S_{ij} is symmetric, only real values exist and thus the points lie only below this surface. In the case of incompressible flow ($I_s = 0$),

$$III_s = \pm \frac{2}{3\sqrt{3}}(-II_s)^{3/2}, \quad (22)$$

which is indicated by the solid curve in Figure 8. The data points show that III_s is primarily positive and, from (19), is consistent with the fact that $\beta > 0$ at most locations. As discussed by Chen *et al.* (1990) and Cantwell (1992), data at high values of $S_{ij}S_{ij}$ (high kinetic energy dissipation) appear to follow the functional form of (22),

$$\frac{II_s}{(27/4 III_s^2)^{1/3}} = -K, \quad (23)$$

where a value of the constant $K = 1.4$ corresponds to the observed 3:1:−4 ratio (Cantwell, 1992). In our decaying homogeneous flow (Figure 8), points at high $S_{ij}S_{ij}$ tend to lie between the curves given

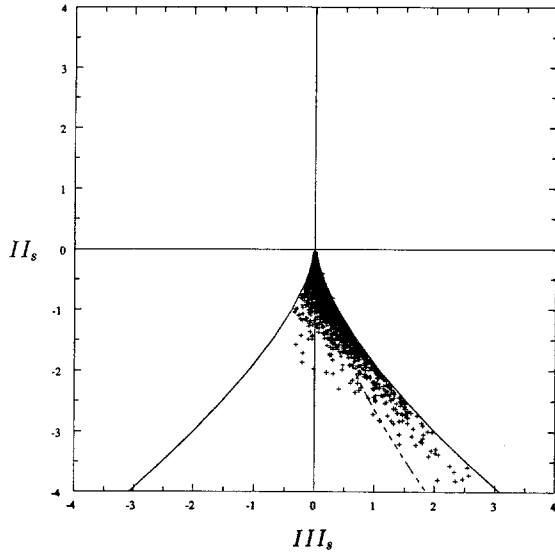


Figure 8. Scatter plot of second and third invariants of the rate-of-strain tensor (II_s-III_s) at time $t = 3.0$ (base sample for six $(x-z)$ planes) for a flow with no energy release (constant density). —, equation (22); ---, equation (23) with $K = 1.4$.

by (23) for $K = 1.4$ (indicated by the dashed line) and (22). Note that solutions given by (22) represent those with real eigenvalues in which at least two have equal values which, for $\beta > 0$, corresponds to $\alpha = \beta$. This is also indicated in Figure 6(b) where the peaks of the α and β distributions have shifted toward each other. The other limiting condition of this region is the case of $III_s = 0$ (the negative y -axis) which can be given by a situation where $\beta = 0$; corresponding to locally two-dimensional straining. This condition is not observed at high dissipation rates. Based on the results of Chen *et al.* (1990) and Sondergaard *et al.* (1991) for various shear flows and our results for homogeneous shear flow (unpublished), it appears that net enstrophy production by vortex stretching (with mean shear) is required to exhibit the relation given by (23). This may be due to the increased correlation between the vorticity and strain fields resulting from this process.

In the case of variable density, since the first invariant I_s is nonzero, the flow no longer resides solely in the II_s-III_s plane. Figure 9 shows points *projected* on the II_s-I_s plane indicating the relative

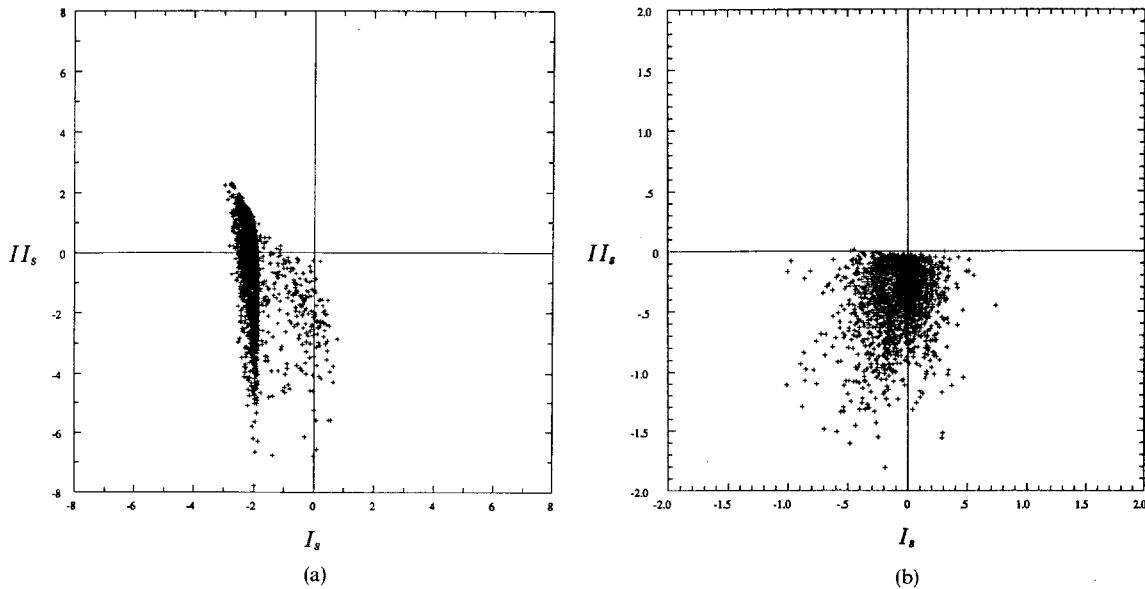


Figure 9. Scatter plots of first and second invariants of the rate-of-strain tensor (II_s-I_s) for a flow with energy release ($0.4 \leq F \leq 0.6$): (a) $t = 0.25$, (b) $t = 3.0$.

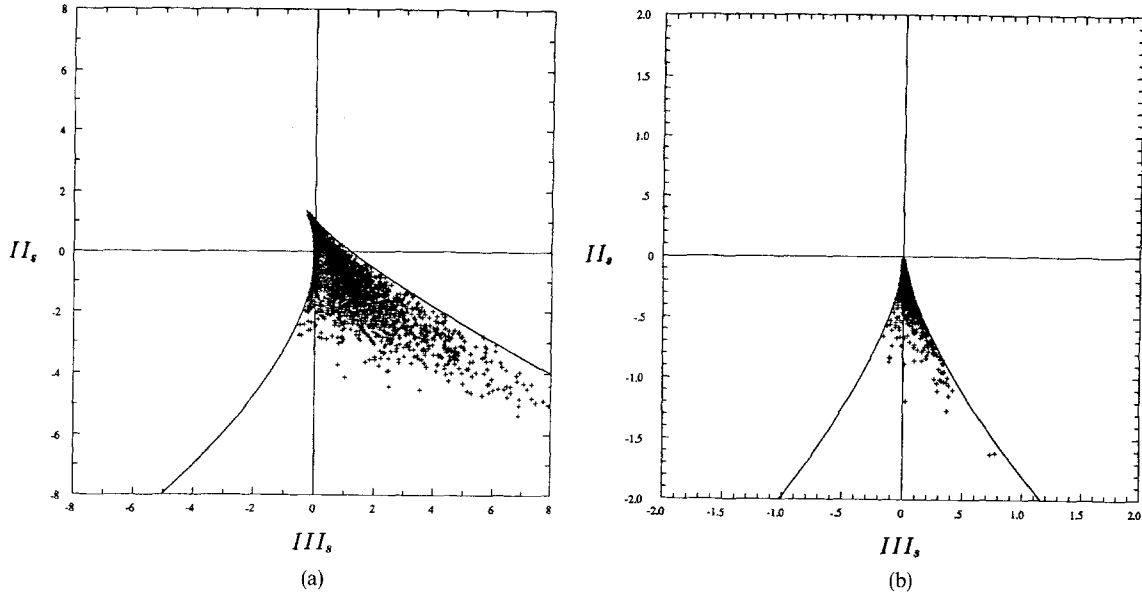


Figure 10. Scatter plots of second and third invariants of the rate-of-strain tensor ($II_s - III_s$) for a flow with energy release at locations where $0.4 \leq F \leq 0.6$: (a) $t = 0.25$, $\bar{I}_s = -2.0$, (b) $t = 3.0$, $\bar{I}_s = -0.1$. —, equation (21).

significance of I_s for a range of F values $0.4 \leq F \leq 0.6$ at two different times. At the earlier time ($t = 0.25$), the presence of $I_s < 0$ due to a positive velocity divergence is apparent. As the flow develops ($t = 3.0$), the magnitude of the divergence diminishes. Figure 10 shows the corresponding data in the $II_s - III_s$ plane limited to those points with $I_s = \bar{I}_s$ of the data in Figure 9. Also included in the plots are the curves corresponding to (21) for the given I_s value. In general, high negative values of II_s are eliminated due to the presence of compressible dissipation S_{ii}^2 (15). Early in the development (Figure 10(a)), there is significant extensional straining and points where $\beta < 0$ are rare. At a later time (Figure 10(b)), the appearance of the plot is more like that of Figure 8. Points lie primarily in the

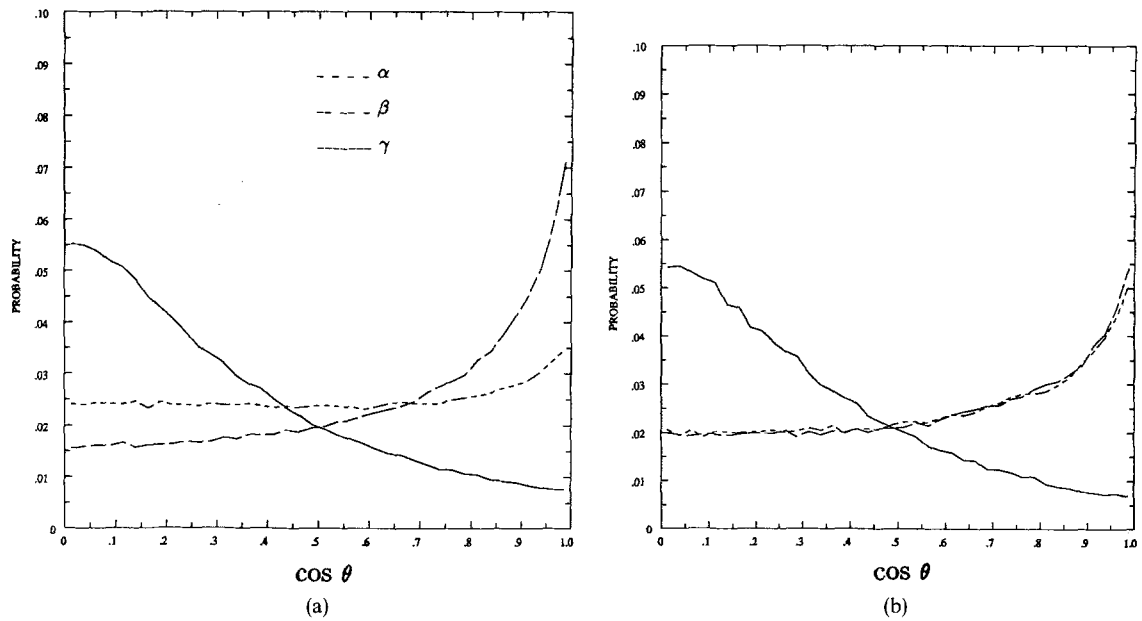


Figure 11. Probability distributions of alignment of the vorticity vector and principal rate-of-strain eigenvectors for base sample ($0.1 \leq F \leq 0.9$) at $t = 3.0$. —, e_γ ; ---, e_β ; - · - ·, e_α . (a) No energy release, (b) with energy release.

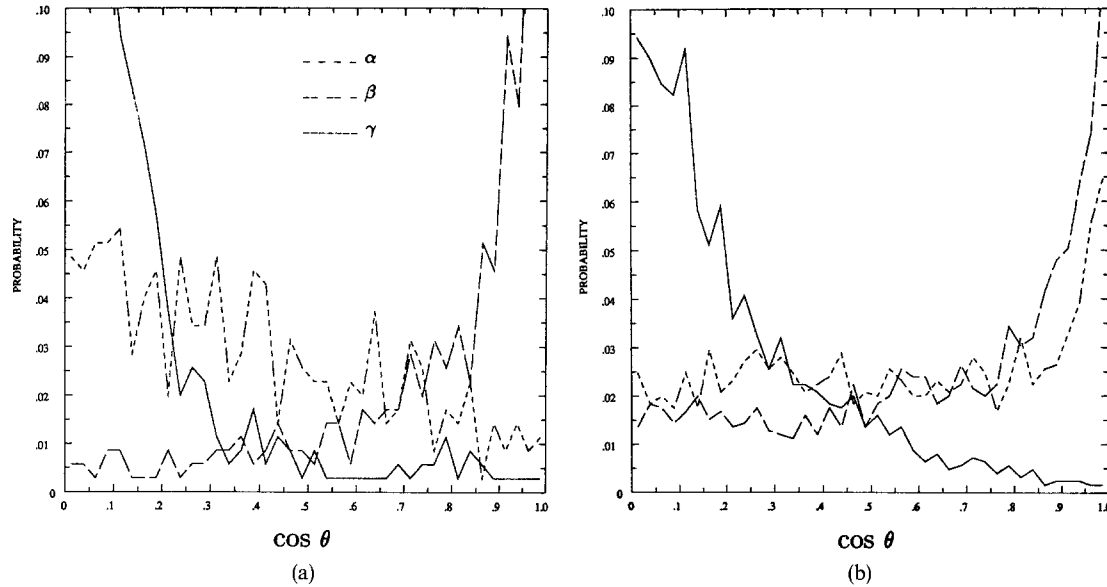


Figure 12. Probability distributions of alignment of the vorticity vector and principal rate-of-strain eigenvectors for high enstrophy locations ($\omega^2 > 8\overline{\omega^2}$) at $t = 3.0$. —, e_γ ; - · -, e_β ; - - - -, e_α . (a) No energy release, (b) with energy release.

$III_s > 0$ region due to the predominance of $\beta > 0$ points. As in the constant density case, at the moderate to high values of I_s , the points tend toward the bounding surface (21).

The preferential orientation of the vorticity vector ω relative to the principal strain axes is determined by evaluating the cosine of the angle between the vorticity vector and the eigenvectors at each grid point. Probability distributions of the direction cosines for both constant- and variable-density conditions for the base sample are shown in Figure 11. The tendency for vorticity to align in the direction of a *positive* eigenvector exists in both cases. This is consistent with the predominance of stretching versus compressing vorticity. In the constant-density case (Figure 11(a)), the preferred alignment of the vorticity with the direction of the intermediate eigenvector e_β is observed. However, in the case with energy release (Figure 11(b)), the statistics show high probability of alignment with both e_α and e_β . If the statistics are recomputed by limiting the sample to those points with high enstrophy or high strain magnitude, alignment characteristics become much more distinct. Figure 12 shows the conditioned probabilities for high enstrophy ($\omega^2 > 8\overline{\omega^2}$) regions. In the constant-density flow (Figure 12(a)), the preference for alignment with e_β and normal orientation with e_γ is enhanced significantly. Furthermore, a preferred normal orientation with respect to e_α is exhibited. In the flow with energy release (Figure 12(b)), a distinction between the profiles of e_α and e_β is exhibited and the preferred alignment of ω with e_β is revealed.

These kinematic features and their corresponding structure can be examined via three-dimensional visualizations of the flow field. Figure 13 shows a typical structure at high vorticity magnitude in the constant-density flow. The perspective shows vortex lines, the color of which indicates local magnitude (blue = low, green = moderate, yellow = high). We see that in the region of highest magnitude (yellow: $\omega > 3\overline{\omega}$), the lines collimate together and form tube-like structures. In this region the eigenvectors e_γ and e_α orient normal to the axis of the structure, as shown by the straight red and yellow lines indicating the magnitudes of γ , α and the directions of e_γ , e_α , respectively. The length of this structure is approximately of the order of the integral lengthscale, and the width of the order of the Kolmogorov lengthscale. Since the highest strain component (γ) is negative and oriented in the normal plane, at high magnitudes of vorticity, the rate of rotation of the strain axes may be large enough to produce a net compressive strain acting normal to the vortex axis, causing the vortex lines to cohere. In fact, there appears to be a helical structure in the vorticity itself as we see a twisting of the vortex lines within the tube-like structure, a feature observed by She *et al.* (1990).

At moderate levels of vorticity, the structural nature is sheet-like. Figure 14 shows a typical structure with the corresponding directions of e_γ (\rightarrow) and e_α (\rightarrow). As in the case of tube-like structures, e_γ and e_α are normal to the local vorticity vectors, however, they are found to orient at

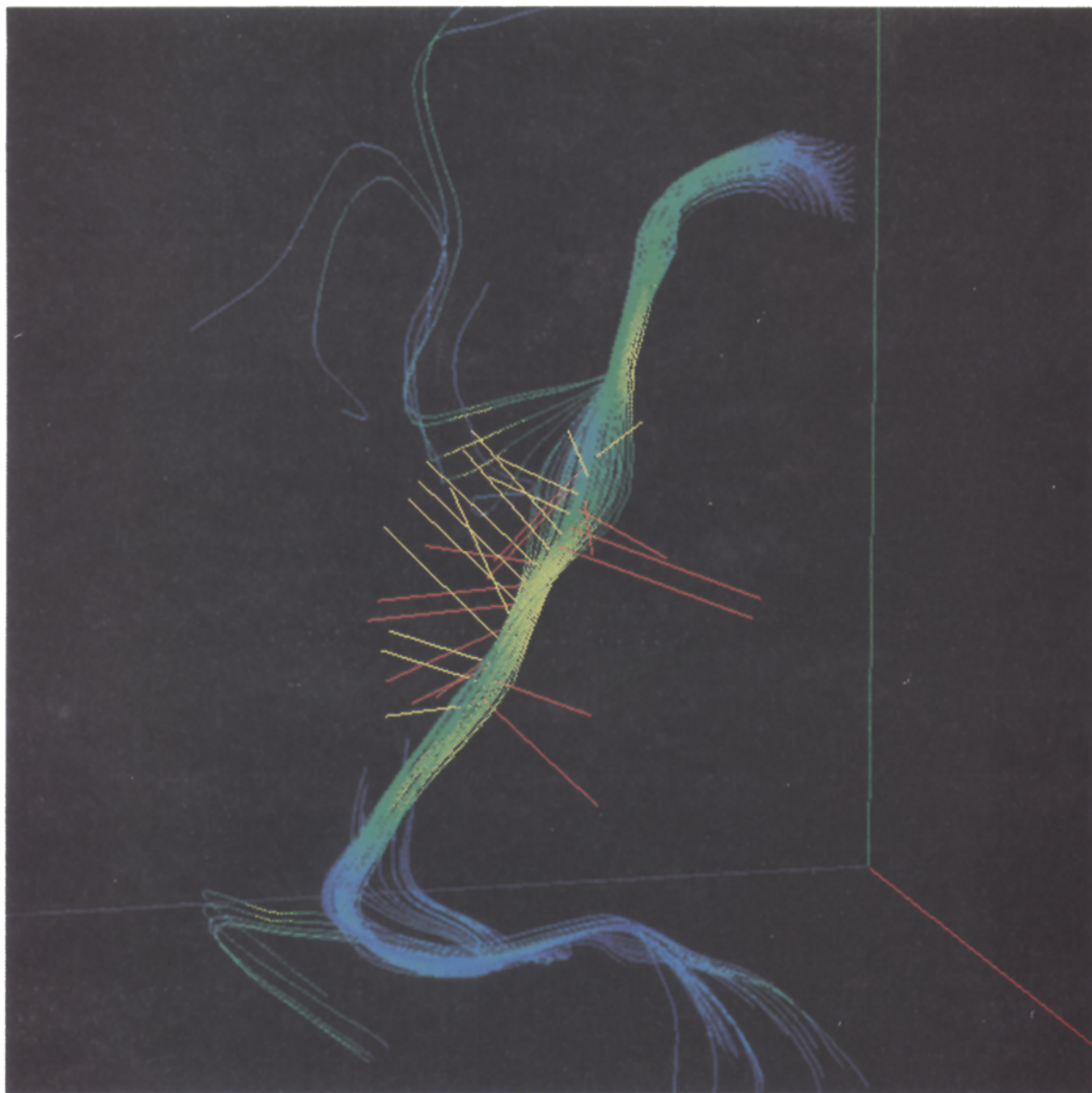


Figure 13. Three-dimensional visualization of vortex lines in a flow with no energy release (constant density) indicating a tube-like structure ($t = 3$). The color of these lines represents the magnitude of ω (yellow = high, green = medium, blue = low). The straight red and yellow lines indicate the orientation of the local principal rate-of-strain eigenvectors, e_γ and e_α , respectively.

approximately 45° angles with respect to the sheet as shown in Figure 14(b) which displays a side view of Figure 14(a). This is also indicated by the alignment probabilities of the scalar gradient (∇F) with the principal eigenvectors (Nomura and Elghobashi, 1993). In general, the scalar gradient tends to orient in the direction of e_γ and normal to e_α and e_β and exists as sheets in the vicinity of sheet-like vortex structures (Nomura and Elghobashi, 1992). However, at moderate to high enstrophy regions, the alignment probability curves of e_γ and e_α exhibit peaks at $\cos \theta = 0.7$ or $\theta = 45^\circ$. This preferred orientation, which is characteristic of a uniform shear flow, was also observed by Ruetsch and Maxey (1992) in their simulations with forced isotropic turbulence. They suggest that tube-like structures are formed from vortex sheets through a Kelvin–Helmholtz-type instability.

In the case of energy release, the preference for vorticity to align with the intermediate eigenvector becomes apparent at high enstrophy or high strain regions. However, as seen in Figure 12(b), there is still a greater probability for vorticity to align with e_α than to orient normal to it. Since the flow

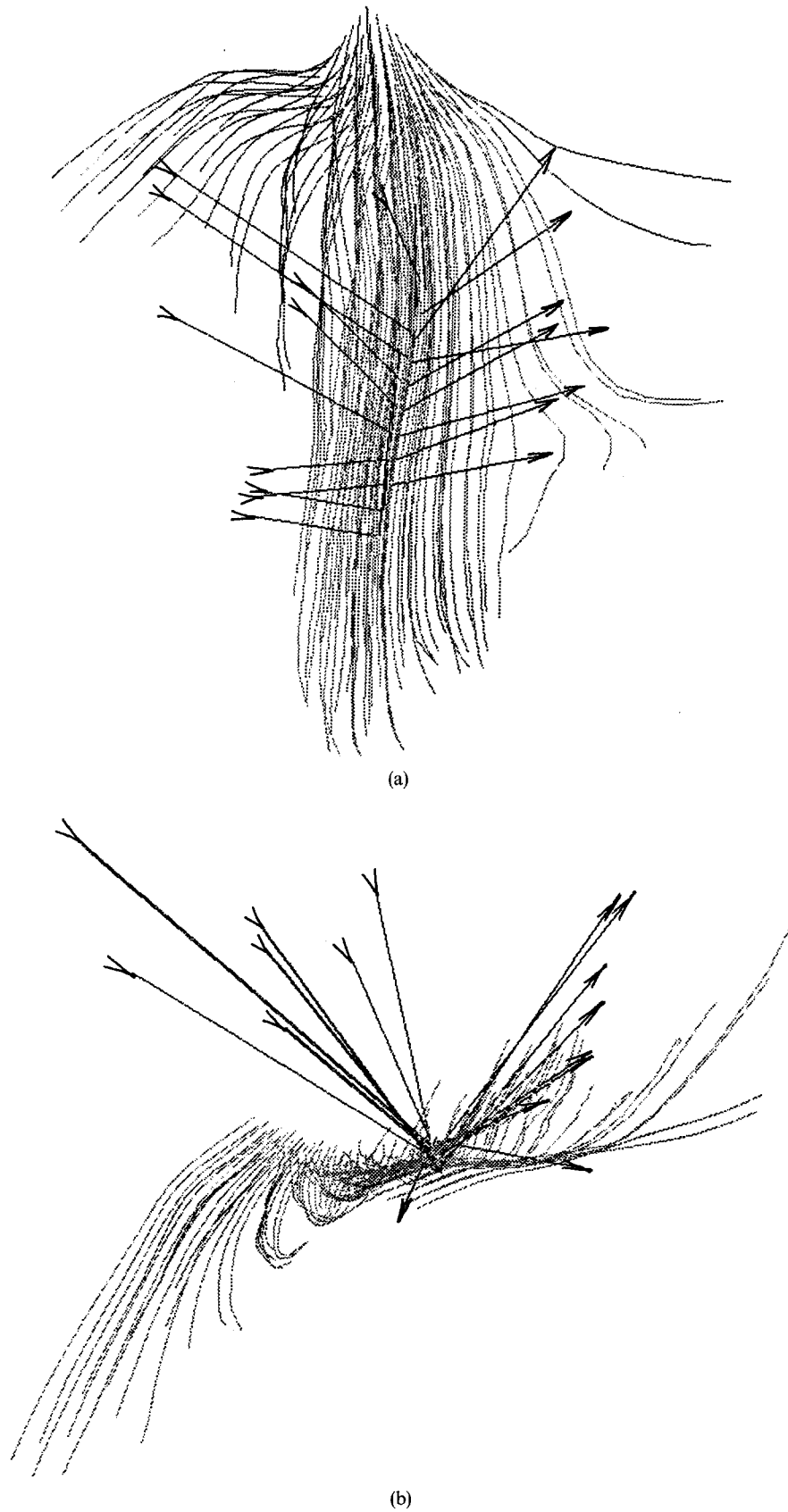


Figure 14. Three-dimensional visualization of vortex lines in a flow with no energy release (constant density) indicating a sheet-like structure ($t = 3$). The straight lines indicate the orientation of the local principal rate-of-strain eigenvectors, e_y (\rightarrow) and e_x (\leftarrow). (a) Frontal view, (b) end view.

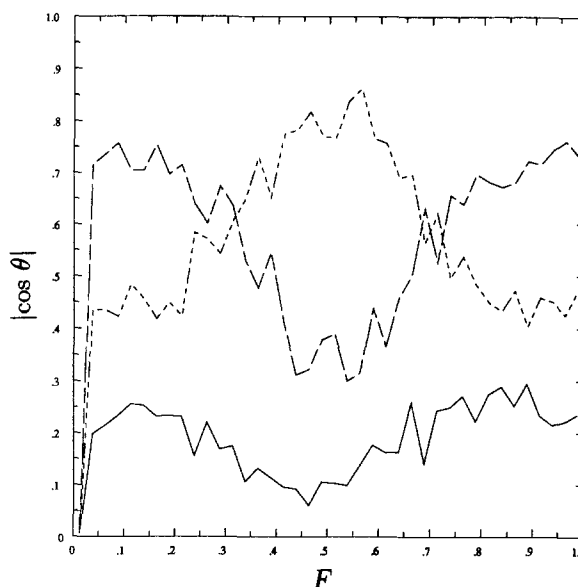


Figure 15. Expected alignment of the vorticity vector and principal rate-of-strain eigenvectors ($|\cos \theta|$) conditioned on the value of the mixture fraction F for high enstrophy locations ($\omega^2 > 8\bar{\omega}^2$) at $t = 3.0$ for a flow with energy release. —, e_γ ; ---, e_β ; - · - ·, e_α .

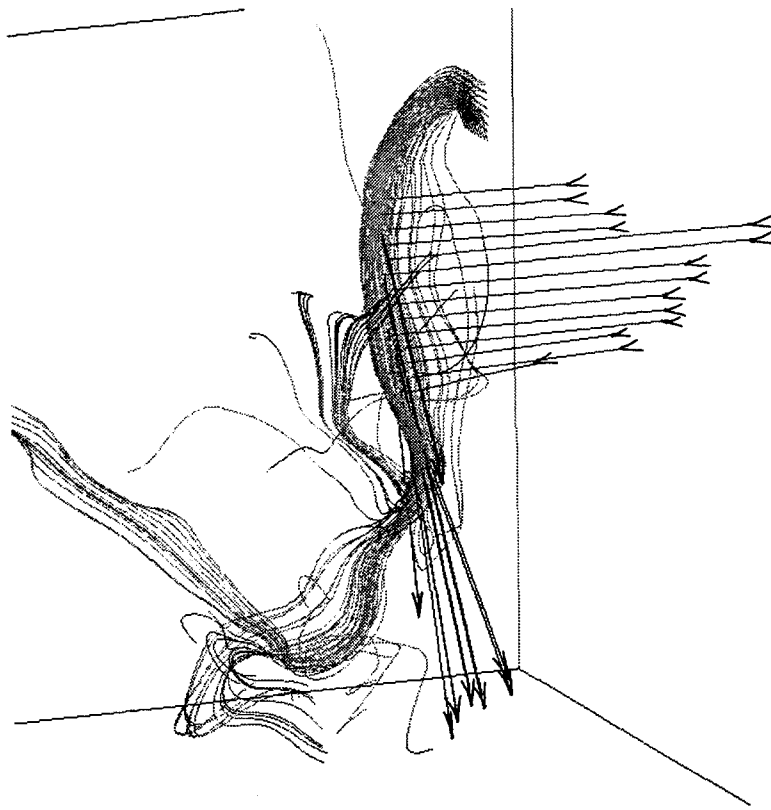
inhomogeneity arises from the scalar field, it is expected that the alignment probabilities may vary with the value of F . Figure 15 shows the expected values for $|\cos \theta|$ conditioned on F at high enstrophy locations. We find that in the central region of the reactive zone where extent of reaction is greatest ($F \simeq 0.5$), there is a greater tendency for ω to align with e_α rather than e_β , while in the outer regions alignment with e_β is preferred (Nomura and Elghobashi, 1993).

A three-dimensional visualization of a region of high magnitude vorticity in the case with energy release is shown in Figure 16. In general, high magnitude vortex structures in the heated flow field are elongated and flattened, resembling ribbons. Since the intensity of vorticity is reduced in the heated (variable-density) flow, tube-like structures are less likely to be present. If indeed a tube-like structure is formed and maintained by the action of a net compressive strain normal to ω , we would expect that this situation is unlikely to occur under conditions of thermal expansion due to the positive shift in the distribution of principal strains. In particular, if we examine the distribution at those points in the flow where ω strongly aligns with e_β ($\cos \theta > 0.99$, Figure 17(b)), we find that the magnitude of γ does not dominate over α as it does in the case of a constant-density flow (Figure 17(a)) and thus a net compressive strain normal to ω does not tend to occur. In the structure shown in Figure 16(a), the local vorticity is aligned with e_α (\rightarrow). Within this region, e_γ (\rightarrow) tends to orient uniformly in one direction and orthogonal to the plane of sheet (Figure 16(b), which would tend to flatten an existing tube-like structure. A sheet-like structure is shown in Figure 18. Here, the preference for e_γ and e_α to orient at 45° to the sheet is eliminated due to the alignment of ω with e_α . The instability mechanism proposed by Ruetsch and Maxey (1992) would therefore be unlikely to occur, resulting in the lack of tube formation.

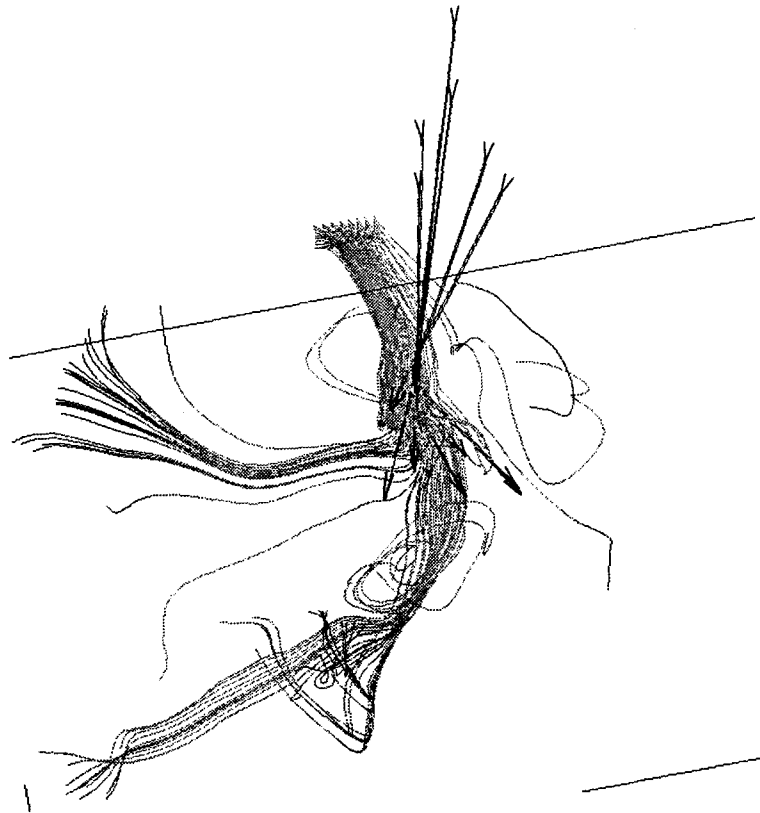
If we look at the expected magnitudes of vorticity $|\omega|$ and total strain-rate ($|e| = (\alpha^2 + \beta^2 + \gamma^2)^{1/2}$) conditioned on alignment with the principal eigenvector directions in the base sample, the highest values (approximately 20% greater than the mean values in each case) occur when orientation of vorticity is with e_β for both the constant- and variable-density flows. In the constant-density case, the expected value of vorticity is uncorrelated with the orientation with respect to e_α . However, in the variable-density case, the highest magnitude vorticity in the central region ($0.4 \leq F \leq 0.6$) occurs when ω aligns with e_α . An indication of the correlation between the strain magnitude and enstrophy is given by the following correlation coefficient:

$$C_{\omega^2 e^2} = \frac{\langle \omega^2 e^2 \rangle}{\langle \omega^2 \rangle \langle e^2 \rangle}, \quad (24)$$

which has an uncorrelated value of 1.0. The constant-density flow has a value of $C_{\omega^2 e^2} = 1.2$ which remains relatively constant. With energy release, the value of $C_{\omega^2 e^2}$ is approximately 1.35–1.4 indicating a slightly higher correlation between e^2 and ω^2 .



(a)



(b)

Figure 16. Three-dimensional visualization of vortex lines in a flow with energy release showing a ribbon-like structure ($t = 3$). The straight lines indicate the orientation of the local principal rate-of-strain eigenvectors, e_y (\rightarrow) and e_x (\rightarrow). (a) Frontal view, (b) end view.

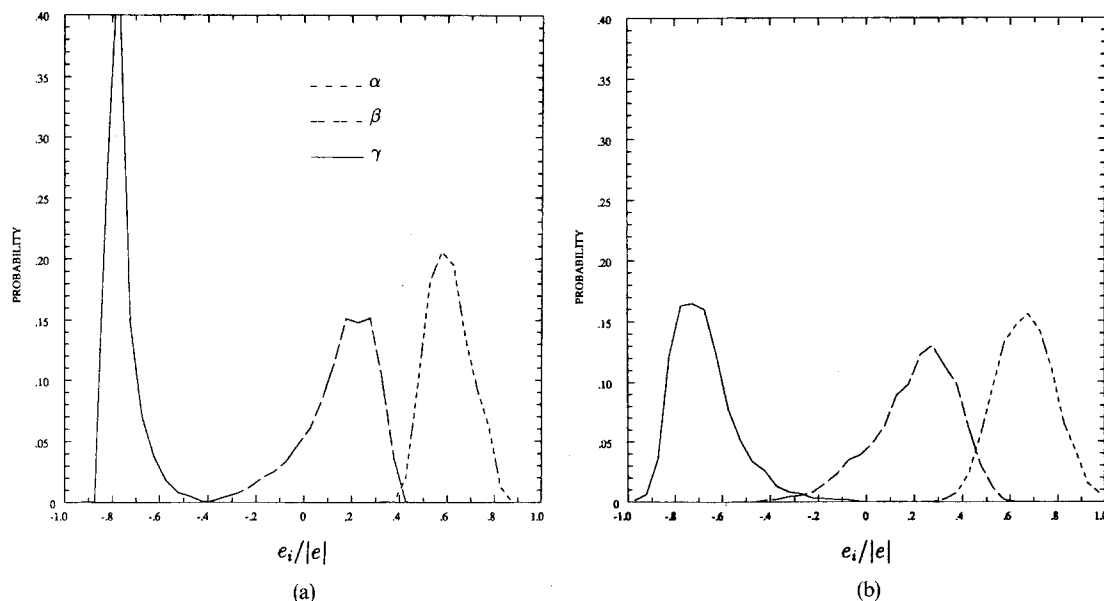


Figure 17. Probability distributions of the principal strain rates normalized by total strain magnitude ($|e| = (\alpha^2 + \beta^2 + \gamma^2)^{1/2}$) for locations where ω aligns with e_β ($|\cos \theta| \geq 0.99$): (a) no energy release, (b) with energy release. —, γ ; ---, β ; ·····, α .

The alignment-conditioned magnitude of the vortex stretching term $\omega_i \omega_j S_{ij}$ shows significantly higher values when ω aligns with e_α in both cases. This is in contrast with sheared turbulence where there is a net production of enstrophy and $\omega_i \omega_j S_{ij}$ is greatest when ω aligns with e_β (Nomura and Elghobashi, 1992). Apparently, vortex stretching in flows with decaying enstrophy tends to be greater when ω is aligned with e_α due to the need for the higher magnitude of strain to compensate for decreasing ω^2 . Since there is a tendency for ω to align with e_α in the flow with energy release, the production of enstrophy by vortex stretching is enhanced in the hottest regions of the flow. Initially, this causes an increase in the z -component of vorticity. However, the average strain and vorticity magnitudes are lower in these regions due to the overall attenuation of turbulence and thus the average production by vortex stretching remains less than that of the cold regions of the flow field. The correlation between ω^2 and e^2 for this orientation is slightly below the mean $C_{\omega^2 e^2} = 1.3$ while the value when ω aligns with e_β is 1.5. It appears that alignment of ω with e_β results in stronger correlation of ω^2 and e^2 .

As stated earlier, when there is exothermic energy release, two additional mechanisms are present in the enstrophy (or vorticity) transport equation. Initially, thermal expansion dominates and this causes the enstrophy to decrease at a faster rate than by viscous effects alone. The average baroclinic torque term in (2) is negative and an order of magnitude less than the expansion term. Beyond this initial period, the flow develops under the competing mechanisms of vortex stretching, dilatation, baroclinic torque, and viscous effects. In regions of highest strain and enstrophy, vortex stretching dominates. In these regions the averaged baroclinic torque term is positive and is significantly above the mean value. As the reactants mix, the product is diluted and thus can locally decrease the density and produce a negative divergence in which locally higher enstrophy can also occur. However, the various contributions to enstrophy production do not exceed the destruction by expansion and viscous effects and therefore the total enstrophy continues to decay in time.

The expected magnitude of the dissipation rate of turbulence kinetic energy ε was also determined and conditioned on vorticity-principal strain-rate alignment. For the base sample, the resulting distributions are similar for both constant- and variable-density flows: ε tends to be highest (40–50% above average value) when alignment is with e_β . In the central region of the heated case, alignment dependency is not as apparent, the expected value of ε is slightly higher when ω aligns with either e_α or e_β .

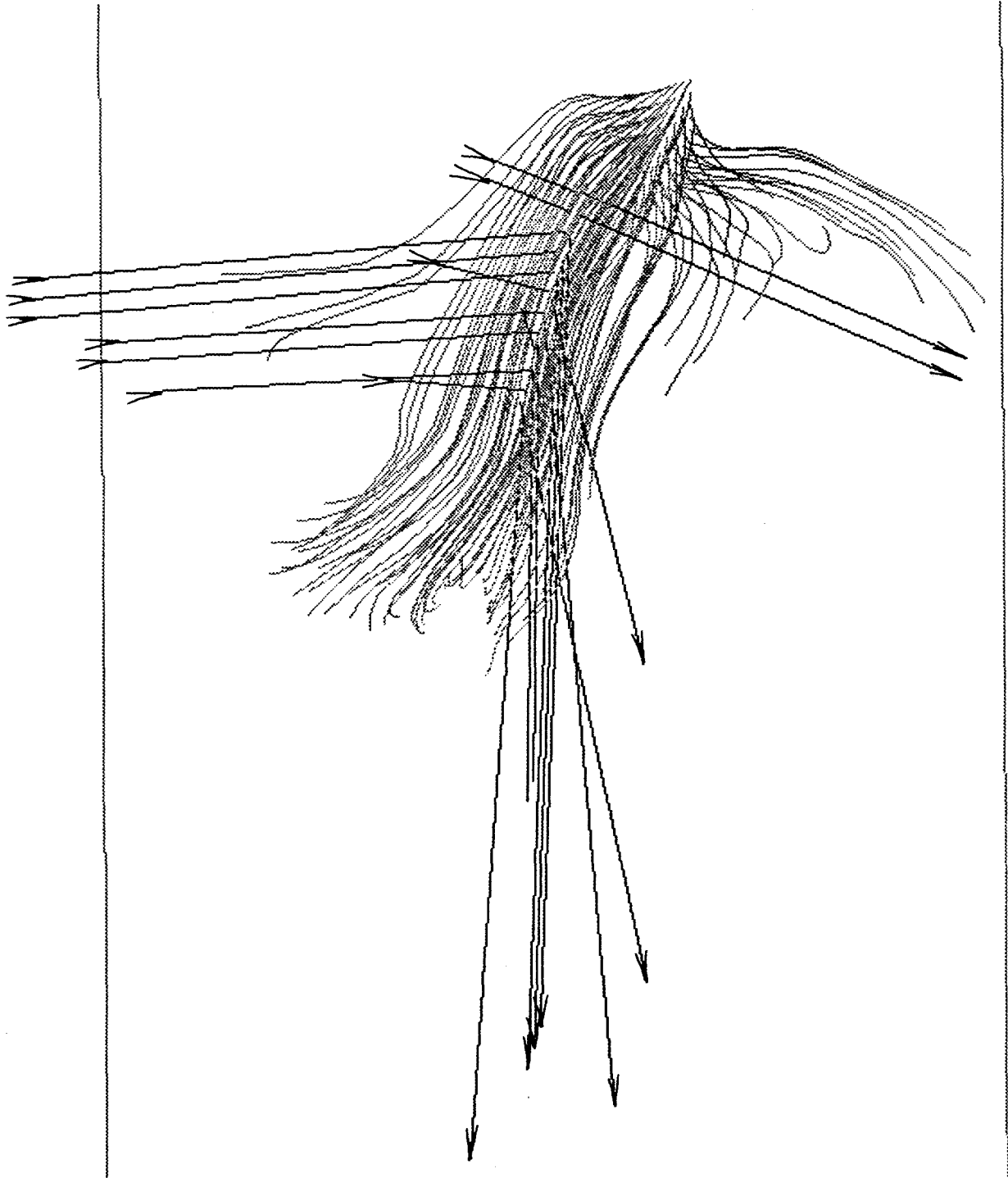


Figure 18. Three-dimensional visualization of vortex lines in a flow with energy release indicating a sheet-like structure (see figure 16 caption for the description).

Topological Characteristics

Topological methods have recently been applied to the description and analysis of flow structure in DNS results (Chen *et al.*, 1990; Sondergaard *et al.*, 1991). These methods are based on critical point concepts (Perry and Chong, 1987) and involve the classification of elementary flow patterns using the three invariants of the velocity-gradient (or rate-of-strain) tensor. This provides a means of assessing and characterizing the nature of a flow field from simulation or experimental data. It must be kept in mind that the analysis is based on a linearized description of the flow and provides the behavior only of *local, instantaneous* streamlines.

In the previous section the invariants of the rate-of-strain tensor were examined (Figures 8–10) to study the nature of the strain field. In order to obtain a complete description of the flow (both irrotational and rotational parts), it is necessary to consider the invariants of the velocity-gradient tensor A_{ij} , which can be expressed in a similar manner as (14)–(16):

$$I = -A_{ii} = -S_{ii}, \tag{25}$$

$$II = \frac{1}{2}(A_{ii}^2 - A_{ij}A_{ji}) = \frac{1}{2}(S_{ii}^2 - S_{ij}S_{ji} - R_{ij}R_{ji}), \tag{26}$$

$$\begin{aligned} III &= -\frac{1}{3!}(A_{ii}A_{jj}A_{kk} - 3A_{ii}A_{jk}A_{kj} + 2A_{ij}A_{jk}A_{ki}) \\ &= \frac{1}{3}(-S_{ii}^3 + 3I(II) - S_{ij}S_{jk}S_{ki} - 3R_{ij}R_{jk}S_{ki}). \end{aligned} \tag{27}$$

The surface dividing the real and complex solutions is again given by (21) in which the subscript s is removed from all terms. Topological classifications are determined by considering the solution trajectories in each of the eigenvector planes. The basic patterns consist of nodes, foci, and saddles. In general, if the eigenvalues are all real, two of the eigenvector planes will contain saddles and the third will contain a node. If the eigenvalues are complex (a pair of complex conjugates and one real root), then a single plane will contain a focus and the solution trajectories spiral around the real eigenvector. The direction of the trajectories is determined by the sign of the real eigenvalues. Figure 19 shows a sketch of possible topologies (local instantaneous streamlines) associated with complex solutions in constant- and variable-density flows. The “spiral” represents a focus and the arrows indicate the direction of the solution trajectories. The additional line shown in the variable-density case indicates where the complex eigenvalues are purely imaginary. A complete description of the various classifications for both incompressible and compressible flows is given by Chong *et al.* (1990).

Figure 20 shows the II – III invariant space corresponding to the velocity-gradient tensor for the constant-density flow. In this case $I = 0$ and the second invariant II (26) reflects the relative magnitudes of $S_{ij}S_{ij}$ ($= S_{ij}S_{ji}$) and $R_{ij}R_{ij}$ ($= -R_{ij}R_{ji}$),

$$II = \frac{1}{2}(-S_{ij}S_{ij} + R_{ij}R_{ij}). \tag{28}$$

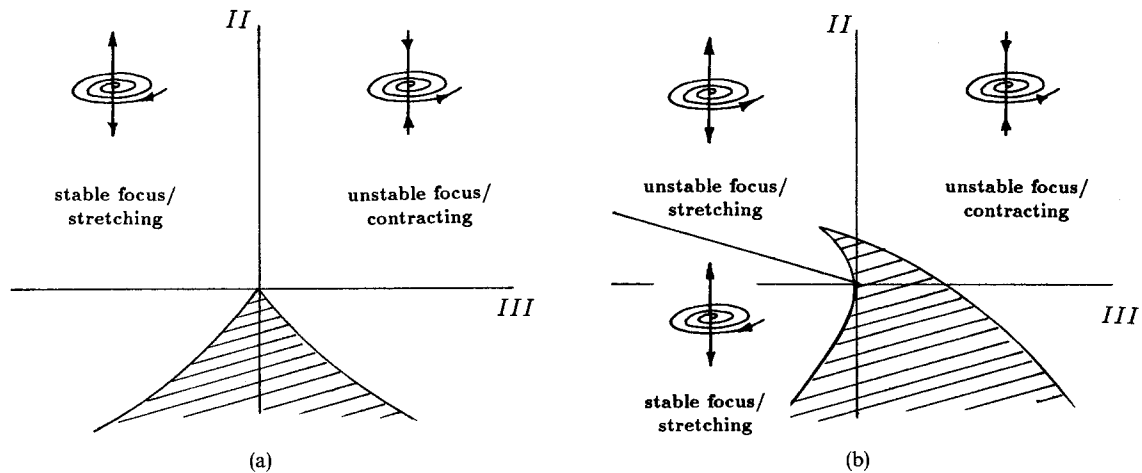


Figure 19. Topological classifications in the II – III plane for (a) $I = 0$ and (b) $I < 0$.

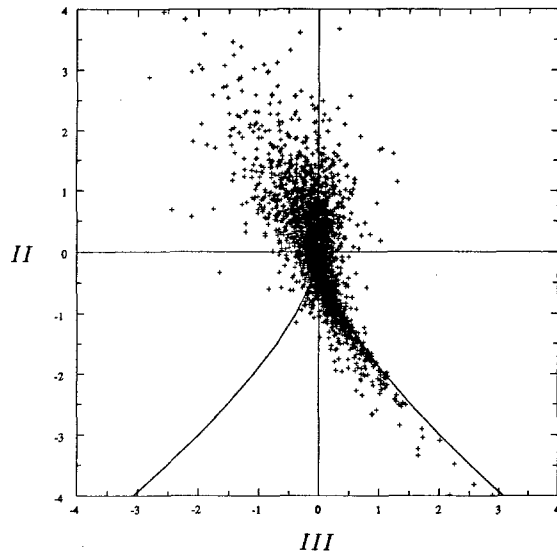


Figure 20. Scatter plot of second and third invariants of the velocity-gradient tensor ($II-III$) for a constant-density flow (no energy release) at time $t = 3.0$ (base sample for six $(x-z)$ planes).

Thus, in the upper plane where $II > 0$, rotation ($R_{ij}R_{ij}$) dominates, and, conversely, in the lower plane $II < 0$, straining ($S_{ij}S_{ij}$) dominates. At large negative II , the data reflect the straining characteristics of Figure 8 which indicates two positive principal strains. At large positive II , the local conditions describe regions of high rotation or enstrophy. As shown in Figure 19, the local streamline pattern suggests the process of vortex stretching. In general, the trends shown here for decaying homogeneous turbulence are similar to those found by Chen *et al.* (1990) and Sondergaard *et al.* (1991) for flows with mean shear.

In a variable-density flow there is a positive contribution from S_{ii}^2 to II , thus the positive II region represents a dominance of the quantity $S_{ii}^2 + R_{ij}R_{ij}$. As discussed, solutions in the upper region are composed of a complex conjugate pair and a real eigenvalue which corresponds to a focus with stretching or contraction in the third direction. Figure 21 shows data points at locations where $0.4 \leq F \leq 0.6$ with values of $I = \bar{I}$ for this F range at two different times. At the early time ($t = 0.25$),

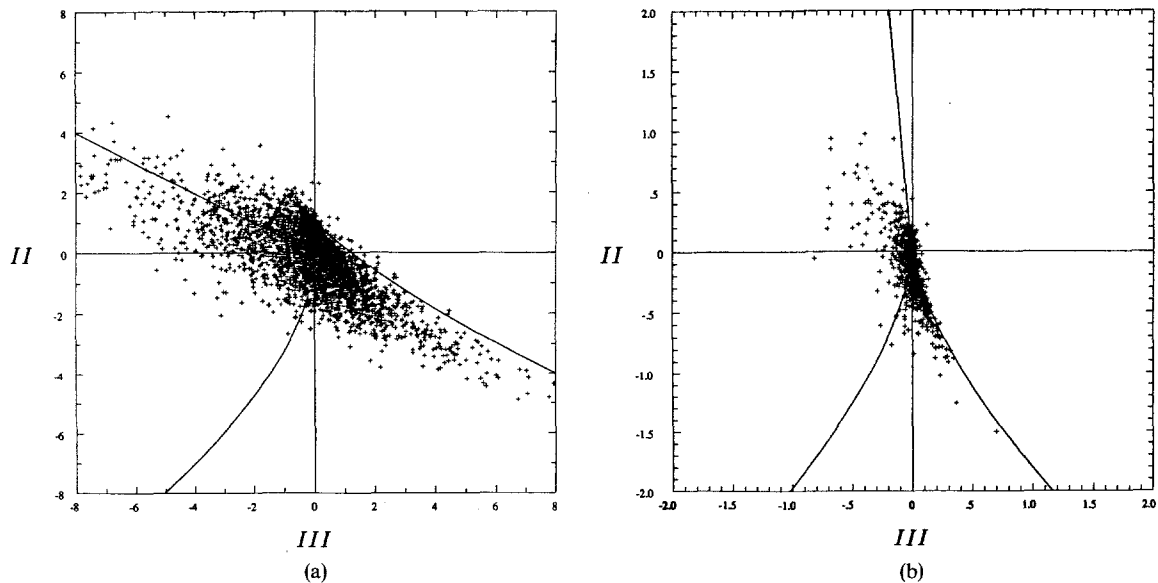


Figure 21. Scatter plot of second and third invariants of the velocity-gradient tensor ($II-III$) for a flow with energy release ($0.4 \leq F \leq 0.6$). (a) $t = 0.25$, $\bar{I} = -2.0$, (b) $t = 3.0$, $\bar{I} = -0.1$.

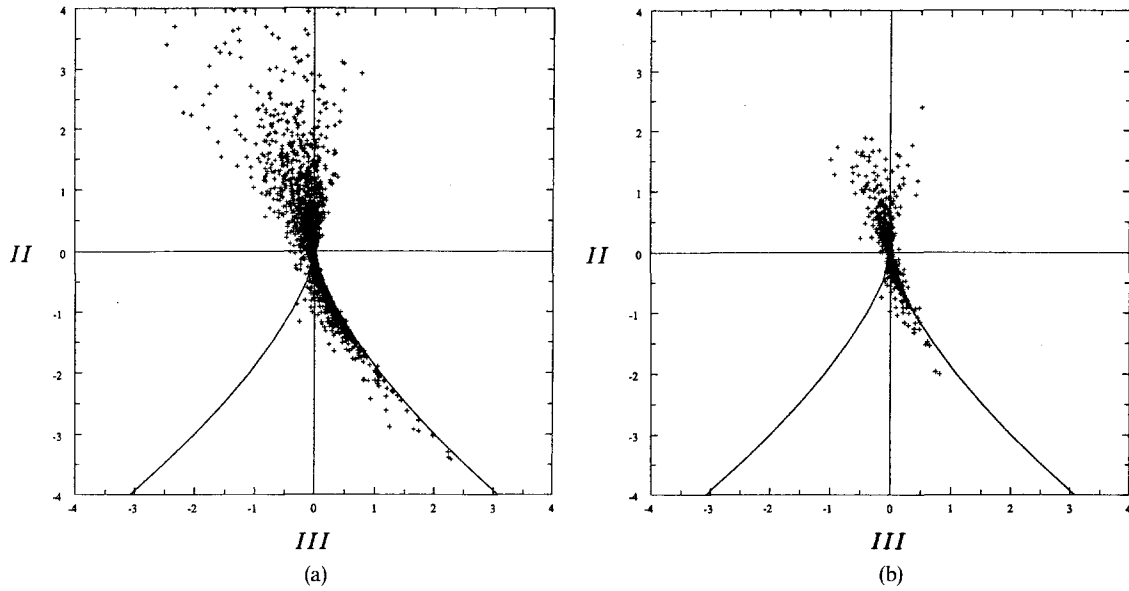


Figure 22. Scatter plot of second and third invariants of the velocity-gradient tensor ($II-III$) conditioned on alignment of ω with e_β ($|\cos \theta| \geq 0.99$) at time $t = 3.0$: (a) no energy release, (b) with energy release.

the dominating effect of the expansion is evident. The upper plane includes both stable and unstable focus/stretching topology. Note that the unstable focus/stretching pattern does not exist in a constant-density flow due to the incompressibility constraint. The flow pattern associated with this topology (Figure 19) suggests a local condition where vortex stretching occurs in the presence of a volume source. In this case the increase in rate of rotation by stretching is inhibited by an increase in fluid volume. At a later time in the development ($t = 3.0$), the velocity divergence is significantly less, and the topology of the upper plane is predominantly stable focus/stretching, similar to that of a constant-density flow.

The topological characteristics associated with the preferred alignment between the vorticity and principal strain are shown in Figures 22 and 23. Figure 22(a) corresponds to the constant-density flow and includes only those points where ω aligns strongly with e_β ($\cos \theta \geq 0.99$). The plot displays a slightly different character than that of Figure 20, particularly near the origin where the values of

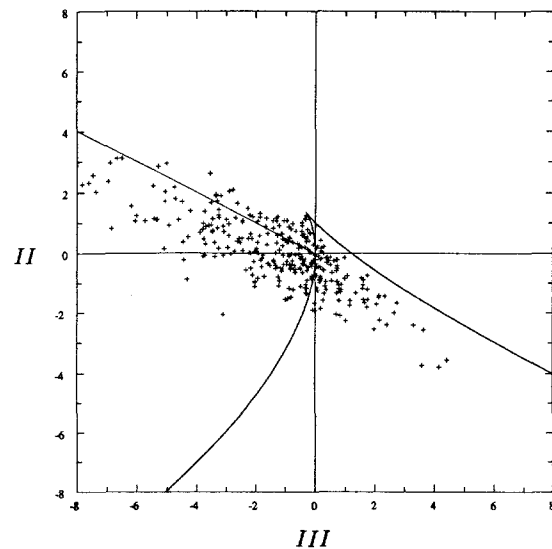


Figure 23. Scatter plot of second and third invariants of the velocity gradient tensor ($II-III$) conditioned on alignment of ω with e_x for a flow with energy release ($0.4 \leq F \leq 0.6$) at time $t = 0.25$.

both invariants tend toward zero. A plot for the variable-density case where ω aligns with e_β exhibits similar characteristics (Figure 22(b)). Finally, Figure 23 contains those points in the central reaction zone ($0.4 \leq F \leq 0.6$) at an early time ($t = 0.25$) where ω aligns with e_α and shows a preference for stable focus/stretching. The higher rate of stretching provided by α is able to overcome volume-expansion effects and results in the higher vortex stretching rates associated with this orientation.

4. Conclusions

In general, in a nonpremixed reacting flow with exothermic energy release, since the intensity of vorticity is reduced and the distribution and alignment characteristics of the principal strains are modified, tube-like structures are less likely to be present. Ribbons and sheet-like structures occur at the relatively high enstrophy regions of the reaction zone. Preferred orientation of the vorticity vector depends on the value of the active scalar (mixture fraction). Regions associated with the greatest extent of reaction ($F \simeq 0.5$) show preferential orientation of ω with the most extensional eigenvector (e_x). Preferential alignment with the intermediate eigenvector e_β is exhibited where F is near the unmixed values (0 and 1) and at regions of highest enstrophy and strain. At the high strain regions, the structure of the principal strain eigenvalues is similar to that of constant-density decaying turbulence at high strain. Although the alignment of ω and e_x may result in locally high enstrophy production by vortex stretching, the counteracting effects of expansion, viscous diffusion, and dissipation result in net enstrophy reduction. The effectiveness in correlating ω^2 and e^2 is also reduced for this orientation. The topological characteristics of flow with energy release reflect the presence of nonzero velocity divergence and show features not present in incompressible flows. In particular, conditions in which vortex stretching is inhibited by the presence of volume expansion is observed. As the flow develops, the divergence decreases and the topological characteristics become similar to those of incompressible turbulence.

Acknowledgments

The authors would like to thank Dr. Alan Shiano for his assistance in the three-dimensional visualization. The computations were performed on the Cray-YMP at the San Diego Supercomputing Center (SDSC).

References

- Aris, R. (1989). *Vectors, Tensors, and the Basic Equations of Fluid Mechanics*. Dover, New York.
- Ashurst, W.T., Kerstein, A.R., Kerr, R.M., and Gibson, C.H. (1987). Alignment of vorticity and scalar gradient with strain rate in simulated Navier–Stokes turbulence. *Phys. Fluids*, **30**, 2343–2353.
- Batchelor, G.K. (1967). *An Introduction to Fluid Dynamics*. University Press, Cambridge.
- Bilger, R.W. (1989). Turbulent diffusion flames. *Ann. Rev. Fluid Mech.*, **21**.
- Burke, S.P., and Schumann, T.E.W. (1928). Diffusion flames. *Indust. Engrg. Chem.*, **20**, 998.
- Cantwell, B.J. (1992). Exact solution of a restricted Euler equation for the velocity gradient tensor. *Phys. Fluids A*, **4**(4), 782–793.
- Chen, J.H., Chong, M.S., Soria, J., Sondergaard, R., Perry, A.E., Rogers, M., Moser, R., and Cantwell, B.J. (1990). A study of the topology of dissipating motions in direct simulation simulations of time-developing compressible and incompressible mixing layers. *Proceedings of the Summer Program*, Center for Turbulence Research, 1990, pp. 139–161.
- Chong, M.S., Perry, A.E., and Cantwell, B.J. (1990). A general classification of three-dimensional flow fields. *Phys. Fluids A*, **2**(5), 765–777.
- Gerz, T., Schumann U., and Elghobashi, S. (1989). Direct numerical simulation of stratified homogeneous turbulent shear flows. *J. Fluid Mech.*, **200**, 563–594.
- Kerr, R.M. (1987). Histograms of helicity and strain in numerical turbulence. *Phys. Rev. Lett.*, **59**, 783–786.
- Lumley, J.L. (1970). *Stochastic Tools in Turbulence*. Academic Press, New York.
- McMurtry, P.A., Riley, J.J., and Metcalfe, R.W. (1989). Effects of heat release on the large-scale structure in turbulent mixing layers. *J. Fluid Mech.*, **199**, 297–332.
- Momtaz, S.W. (1990). Direct Simulation of Homogeneous Turbulence in Sheared and Unsheared Stratified Compressible Flows. Master's Thesis, University of California, Irvine, CA.

- Nomura, K.K., and Elghobashi, S.E. (1992). Mixing characteristics of an inhomogeneous scalar in isotropic and homogeneous sheared turbulence. *Phys. Fluids A*, **4**, 606–625.
- Nomura, K.K., and Elghobashi, S.E. (1993). Small-scale characteristics of a conserved scalar in a turbulent exothermic reacting flow, submitted to *Phys. Fluids*.
- Paolucci, S. (1982). On the filtering of sound from the Navier–Stokes equations. Report SAND82-8257, Sandia National Laboratories, Albuquerque, NM.
- Perry, A.E., and Chong, M.S. (1987). A description of eddying motions and flow patterns using critical-point concepts. *Ann. Rev. Fluid Mech.*, **19**, 125–155.
- Ruetsch, G.R., and Maxey, M.R. (1991). Small-scale features of vorticity and passive scalar fields in homogeneous isotropic turbulence. *Phys. Fluids A*, **3**, 1587–1597.
- Ruetsch, G.R., and Maxey, M.R. (1992). The evolution of small-scale structures in homogeneous isotropic turbulence. *Phys. Fluids A*, **4**, 2747–2760.
- She, Z-S., Jackson, E., and Orszag, S.A. (1990). Intermittent vortex structures in homogeneous isotropic turbulence. *Nature*, **344**, 226–228.
- She, Z-S., Jackson, E., and Orszag, S.A. (1991). Structure and dynamics of homogeneous turbulence: models and simulations. *Proc. Roy. Soc. London Ser. A*, **434**, 101–124.
- Sondergaard, R., Chen, J., Soria, J., and Cantwell, B. (1991). Local topology of small scale motions in turbulent shear flows. *Proceedings of the Eighth Symposium on Turbulent Shear Flows*, Munich, p. 16-1-1.
- Tsinober, A., Kit, E., and Dracos, T. (1992). Experimental investigation of the field of velocity gradients in turbulent flows. *J. Fluid Mech.*, **242**, 169–192.
- Vincent, A., and Meneguzzi, M. (1991). The spatial structure and statistical properties of homogeneous turbulence. *J. Fluid Mech.*, **225**, 1–20.
- Zeldovich, Y.B. (1949). On the theory of combustion in initially unmixed gases. *Zh. Tekhn. Fiz.*, **19**, 10. English translation (1950), N.A.C.A. Technical Memo No. 1296.